Fuel Cells Bulletin
ISSN: 1464-2859

A Fast Numerical Method for Magnetic Field Analysis of Coaxial Magnetic Gears with Bridge-Connected Modulators Considering Magnetic Saturation

Qianli Mai*, Qingchun Hu

School of Mechanical and Automotive engineering,South China University of Technology, Guangzhou, 510641, China

Corresponding Author's Email: imgaby@foxmail.com

Abstract:
This paper presents a novel approach for calculating the magnetic field distribution of magnetic gears(CMGs) with bridge connection in modulator. The modulator and bridge connection regions were divided into several unit modules to derive a convolution matrix of permeability. The magnetic field distribution was then calculated using spatial harmonic modeling method(SHMM). To accurately account for the influence of nonlinear permeability and saturation on the magnetic field distribution, the permeability curve of the material was incorporated, and the permeability distribution function was modified using an iterative method. To verify the method, the magnetic field distribution of two sets of magnetic gears with different bridge parameters was calculated. The proposed method for accurately calculating the magnetic field distribution of CMGs with bridge connections is validated by comparing it with the results obtained from finite element analysis(FEA).

Keywords: spatial harmonic modeling method, magnetic saturation, coaxial magnetic gear, magnetic field distribution calculation

1. Introduction

Magnetic gear is a non-contact transmission mechanism that modulates the magnetic field generated by the permanent magnet on the rotor is modulated by the magnetic modulator. the modulator change the number of pole-pairs and rotational speed of the permanent magnet will change, and the permanent magnet will be coupled with the magnetic field on the other side to generate transmission torque, thus conducting the same variable speed transmission as the mechanical gear. The magnetic transmission of magnetic gear will not generate any friction loss, which is different from the mechanical gear. Therefore, vibration isolation and transmission sealing can be achieved. Furthermore, its structure will not be damaged even if the torque exceeds the limit value. Fig.1 shows the topology of a typical radial flux rotating coaxial magnetic gear. A CMG consists of three parts , and the two rotors typically are distributed on the inner and outer sides of the modulators. Permanent magnets with alternating magnetization directions are evenly distributed on the surface of rotors.

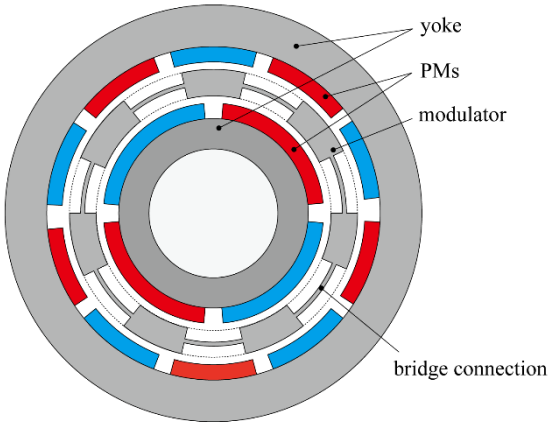

Fig.1 Topologies of CMG

Relevant research results indicate that the inner and outer rotors can generate stable torque under the following conditions:

$$P_i + P_o = N_m \tag{1}$$

where P_i and P_o are pole pairs of two rotors respectively, N_m represents the number of modulating pieces.

In addition, their steady speed and torque also meet the following relationship

$$\frac{n_i - n_m}{n_o - n_m} = -\frac{T_o}{T_i} = K = \frac{P_o}{P_i} \quad (2)$$

where *Ti* and *To* represents torque, *ni*, *no*, *nm* represent the rotation speed, *K* is the gear ratio of CMG.

In recent years, many scholars have studied principle of magnetic field modulation[1],[2] and proposed many new structures, such as Nutation Magnetic Gear[3],[4], Superconductive Magnetic Gear[5], Eccentric Magnetic Harmonic Gear[6],[7], Permanent-Magnet Harmonic Machine[8], Magnetic Field Screw[9]. And the common methods applied to the calculation of magnetic field distribution are as follows : subdomain method[1],[4],[5],[10]-[12], equivalent magnetic circuit network method[13], superposition methods[14], boundary perturbation method[7], differential evolution algorithm[15]. The calculation of magnetic field distribution contributes to optimize the key size in CMG[10],[15], propose a new topological structure[11],[12], Improve electromagnetic performance, such as increasing peak torque, reducing pulsating torque and loss[7],[14]-[17].

Although the effective part of the CMGs seems to have a very simple structure, auxiliary mechanisms such as supporting and fixing components should be considered to ensure the efficient operation of the CMGs during the actual manufacturing process[18],[19]. To maintain the accuracy of the relative positions between the magnetic modulators and reduce the deformation during operation, it is necessary to set a bridge connection between the magnetic modulators. In fact, the bridge connection and the magnetic modulator are usually integrally processed into a thin ring, so that the magnetic modulators are connected one by one. As for the salient-pole magnetic modulator, the structure of its bridge connection will lead to the reduction of the torque transmission capacity of the magnetic gear, although it can enhance the mechanical strength of the modulator[20],[21]. Moreover, any bridge connection with a small size cannot be processed. On the contrary, during the operation of the connection bridge with a large width, numerous magnetic induction lines enter another magnetic modulating block through the connection bridge and return to the original rotor to achieve the magnetic shielding effect. Therefore, the design parameters of the bridge connection will have a significant impact on the magnetic gear.

The size of the bridge connection is usually minimized to reduce the influence of the magnetic shielding effect. If the bridge connection is narrow, the magnetic saturation of the bridge connection and the magnetic modulator will occur frequently during operation, which means that there is additional harmonic that may cause pulsating torque in the magnetic field generated by the magnetic modulator. Most research involving the analysis and calculation of magnetic gears assumes that the magnetic modulator has infinite permeability, which is not applicable to the calculation of the magnetic field with the bridge connection.

2. Analytical Model

2.1 Basic assumption

In order to simplify the calculation model, the following assumptions are made:

(1) the end effects are neglected,and the parameters remain axially symmetric so each component can be expressed in two-dimensional polar coordinates.

(2) The magnetic permeability of the inner and outer yoke is assunmed to be infinite.

(3)The magnetic permeability of the same substance in the same region does not change radially.

(4)The permeability is uniform within a cell unit, but may vary across different regions.

2.2 Model operation principle

In this paper, The modulator of CMG is mainly composed of two parts, the magnet modulating piece and the bridge connection. In order to simplify the calculation, the most typical shape is used,which means each modulating piece has the same radial arc angle, and the bridge connection is shaped like a ring that connects the parts.

As shown in Fig.2, the CMG is divided into seven regions radially. The radius from the inside to the outside are R_1 to R_6, and the corresponding region is region I to region VII. Region III and V represents the part of the modulator without the bridge connection, and region IV represents the radius range of the bridge connection in the modulator. In particular, region III or IV does not exist when the connection bridge area is located inside the modulator ($R_{b\_i}=R_3$) or outside the modulator ($R_{b\_o}=R_4$).

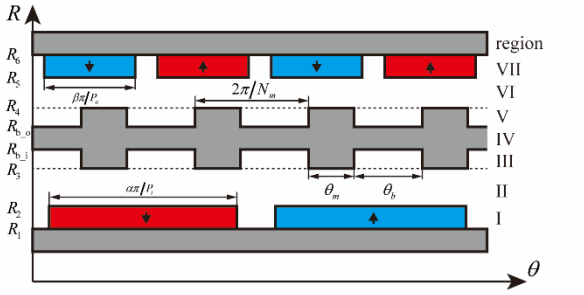

Fig.2 Region division of CMG

The area where the modulator is located, including the bridge connection area and the magnetic adjustment block area without the connection bridge, is divided radially into three layers corresponding to regions III to V. It is also divided tangentially into K modules, as shown in Fig.3, each corresponding to θ_k^j. Furthermore, the magnetic permeability of each unit is independent.

$$\mu^i(\theta_k)=\begin{cases}\mu_k^i,(2n-1)K\le k\le 2nK\\ \mu_0,2nK\le k\le(2n+1)K\end{cases} \tag{3}$$

$$\mu^o(\theta_k)=\begin{cases}\mu_k^o,(2n-1)K\le k\le 2nK\\ \mu_0,2nK\le k\le(2n+1)K\end{cases} \tag{4}$$

where n=1,2…N_m.

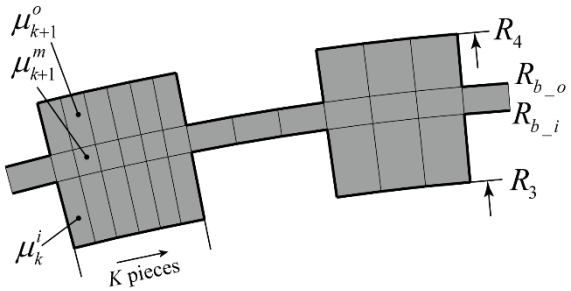

Fig.3 Cell division of modulator

2.3 Magnetic field equation and boundary conditions

In the static field, Ampere's loop theorem and magnetic flux continuity law are respectively given by

$$\nabla\times\vec{H}=\vec{J} \tag{5}$$

$$\nabla\cdot\vec{B}=0 \tag{6}$$

Where $\vec{J}$ refers to the current density. In CMG, $\vec{J}=0$.

The relation between $\vec{B}$ and $\vec{H}$ is given by

$$\vec{B}=\mu\vec{H}+\mu_0\vec{M} \tag{7}$$

where $\vec{M}$ is the residual magnetization.

The relation between $\vec{A}$ and $\vec{B}$ is given by

$$\vec{B}=\nabla\times\vec{A} \tag{8}$$

In two-dimensional field, the vector magnetic potential $\vec{A}$ can be simplified as A_z. The two-dimensional Poisson equation in polar coordinate is as

$$\nabla^2A_z=\frac{\partial^2A_z}{\partial r^2}+\frac{1}{r}\frac{\partial A_z}{\partial r}+\frac{1}{r^2}\frac{\partial^2A_z}{\partial\theta^2}=-\mu_0\nabla\times M \tag{9}$$

In the region without permanent magnet, the right hand side of the equation is zero and becomes Laplace equation.Between each adjacent region, B_r and H_e should be continuous.

$$B_r^{\Omega} = B_r^{\Omega'}\Big|_{r=R_{\Omega,\Omega'}} \text{ and } H_\theta^{\Omega} = H_\theta^{\Omega'}\Big|_{r=R_{\Omega,\Omega'}} \tag{10}$$

where $R_{\Omega,\Omega'}$represents the radius at the junction of two regions and B_r and H_θ can be calculated using the following equations as

$$B_r = \frac{1}{r}\frac{\partial A_z}{\partial \theta} \tag{11}$$

$$H_\theta = \mu_r B_\theta = -\mu_r \frac{\partial A_z}{\partial r} \tag{12}$$

2.4 Magnetic field equation and boundary conditions

Each region's magnetic solution can be represented as a complex Fourier series. In the case of A_z, the complex Fourier series expansion can be expressed as:

$$A_z(r,\theta) = \sum_{n=-N}^{N} \hat{A}_z(r,n)e^{-in\theta} = \mathbf{A}_z \cdot \mathbf{E}^T \tag{13}$$

where $-N \le n \le N$ is the number of harmonics,and $\hat{A}_z$ represents the fourier coefficents of A_z, and the coefficent matrix is given by

$$\mathbf{A}_z = [\hat{A}_{z,-N}(r)\cdots\hat{A}_{z,0}(r)\cdots\hat{A}_{z,N}(r)] \tag{14}$$

$$\mathbf{E} = \left[e^{jN\theta}\cdots 1\cdots e^{-jN\theta}\right] \tag{15}$$

Similarly, we can get the Fourier expansion coefficient matrix of $\mathbf{B}_r$, $\mathbf{B}_\theta$,$\mathbf{H}_r$ and $\mathbf{H}_\theta$.

In this case, surface-mounted and radially magnetized PMs are considered , and the magnetization function is as shown in the Fig4, then the matrix and the Fourier coefficient can be written as[22]:

$$\mathbf{M} = [\hat{M}(-N)\cdots\hat{M}(N)] \tag{16}$$

$$\hat{M}_i(n) = \frac{B_r}{2jn\pi\mu_0} e^{jnP_i\theta_{i0}}(e^{j\alpha n\pi} + e^{jn\pi} - e^{j\alpha n\pi + jn\pi} - 1) \tag{17}$$

where P_i and θ_i are the parameters of inner rotor, and should be replaced by P_o and θ_o in outer rotor.

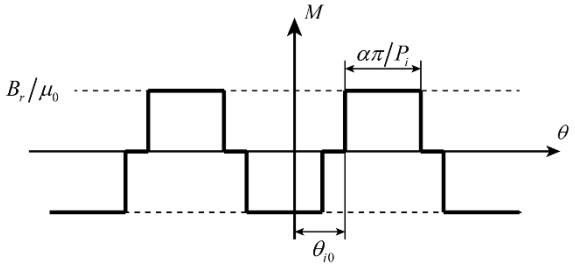

Fig.4 Magnetization distribution of PM region

2.5 Solution of permeability coefficient matrix

The initial value of the permeability of the calculated region are, μ_0 in air and permanent magnet regions, and μ_r in permeability of the iron core material regions. The matrix coefficient of the magnetic permeability in the bridge connection satisfies

$$\hat{\mu}_n^b = \begin{cases} \dfrac{1}{K}\left(\sum_{k=1}^{K}\mu_k^b\right) & n=0 \\ \sum_{k=1}^{K}\dfrac{\mu_k^b}{2jn\pi}\left(e^{-jnT_0}-1\right)e^{-jknT} & n\neq 0 \end{cases} \tag{18}$$

where $T_0=\pi/N_mK$. Similarly, the Fourier coefficients of region III and V can be written as $\hat{\mu}_k^i$, $\hat{\mu}_k^o$. It should be noted that the permeability in the air range is μ_0.

According to Cauchy product theorem, the matrix form in(7) can be written as[23]

$$\mathbf{B}_r = \boldsymbol{\mu}_{cr}\mathbf{H}_r \tag{19}$$

$$\mathbf{B}_\theta = \boldsymbol{\mu}_{c\theta}\mathbf{H}_\theta \tag{20}$$

The coefficients of the convolution matrices are define as

$$\boldsymbol{\mu}_{cr} = \begin{bmatrix} \hat{\mu}_0 & \cdots & \hat{\mu}_{-2N} \\ \vdots & \ddots & \vdots \\ \hat{\mu}_{2N} & \cdots & \hat{\mu}_0 \end{bmatrix} \tag{21}$$

$$\boldsymbol{\mu}_{c\theta} = \begin{bmatrix} \hat{\mu}_0^{rec} & \cdots & \hat{\mu}_{-2N}^{rec} \\ \vdots & \ddots & \vdots \\ \hat{\mu}_{2N}^{rec} & \cdots & \hat{\mu}_0^{rec} \end{bmatrix}^{-1} \tag{22}$$

where $\hat{\mu}_n^{rec} = 1/\hat{\mu}_n$

2.6 Solving equations

The matrix form in(9) can be written as

$$\frac{\partial^2\mathbf{A}_z}{\partial r^2} + \frac{1}{r}\frac{\partial\mathbf{A}_z}{\partial r} - \frac{1}{r^2}\mathrm{U}\frac{\partial^2\mathbf{A}_z}{\partial\theta^2} = 0 \tag{23}$$

$$\frac{\partial^2\mathbf{A}_z}{\partial r^2} + \frac{1}{r}\frac{\partial\mathbf{A}_z}{\partial r} - \frac{1}{r^2}\mathrm{U}\frac{\partial^2\mathbf{A}_z}{\partial\theta^2} = -i\frac{\mu_0}{r}\mathbf{W}\mathbf{M}_r \tag{24}$$

where $\mathbf{U} = \boldsymbol{\mu}_{c\theta}\mathbf{K}_\theta\boldsymbol{\mu}_{cr}^{-1}\mathbf{K}_\theta$

The solution of the Homogeneous matrix equation can be written as

$$\begin{aligned} \mathbf{A}_z &= r^{\mathbf{U}^{\frac{1}{2}}}\mathbf{C}_1 + r^{-\mathbf{U}^{\frac{1}{2}}}\mathbf{C}_2 \\ &= \mathbf{V}r^{\lambda}\mathbf{V}^{-1}\mathbf{C}_1 + \mathbf{V}r^{-\lambda}\mathbf{V}^{-1}\mathbf{C}_2 \\ &= \mathbf{V}\left(r/R_i\right)^{\lambda}\mathbf{X}_1 + \mathbf{V}(r/R_o)^{-\lambda}\mathbf{X}_2 \end{aligned} \tag{25}$$

where $\mathbf{V}$ and λ are eigenvalue and eigenvector of $\mathbf{U}$. Replacing r with r/R_x can effectively avoid overflow of calculation, where R_i and R_i indicates the inner and outer radius of the area.

Thus the solution of the Nonhomogeneous equation is

$$\mathbf{A}_z = \mathbf{V}\left(r/R_i\right)^{\lambda}\mathbf{X}_1 + \mathbf{V}(r/R_o)^{-\lambda}\mathbf{X}_2 + r^2\mathbf{X}_3 \tag{26}$$

where $\mathbf{X}_3 = -(4\mathbf{I}-\mathbf{U})^{-1}i\frac{\mu_0}{r}\mathbf{W}\mathbf{M}_r$

By substituing (11), (12) into (24), the coefficient matrix of the magnetostatic field solution can be written as

$$\mathbf{B}_r = \frac{1}{r}\frac{\partial\mathbf{A}_z}{\partial\theta} = -i\frac{1}{r}\mathbf{K}_\theta\mathbf{A}_z = \mathbf{a}\left(r\right)\cdot\mathbf{X}^T \tag{27}$$

$$\mathbf{B}_\theta = -\frac{\partial \mathbf{A}_z}{\partial r} = -\frac{\lambda}{r}\mathbf{A}_z = \mathbf{b}(r)\cdot\mathbf{X}^T \tag{28}$$

$$\mathbf{H}_r = -i\frac{1}{r}\mu_{cr}^{-1}\mathbf{K}_\theta\mathbf{A}_z = \mathbf{c}(r)\cdot\mathbf{X}^T \tag{29}$$

$$\mathbf{H}_\theta = -\boldsymbol{\mu}_{c\theta}^{-1}\frac{\partial \mathbf{A}_z}{\partial r} = \mathbf{d}(r)\cdot\mathbf{X}^T \tag{30}$$

where the $\mathbf{X} = \left[\mathbf{X}_1^T, \mathbf{X}_2^T, \mathbf{X}_3^T\right]$ represents the matrix coefficient of the region

Substituting B_r and H_θ ,corresponding equation (27) and (29), in each region into the boundary condition (10) and the coefficient matrix corresponding to each region can be solved as

$$\begin{bmatrix} \mathbf{a}^{\mathrm{I}} & -\mathbf{a}^{\mathrm{II}} & \mathbf{0} & \cdots & \mathbf{0} \\ \mathbf{c}^{\mathrm{I}} & -\mathbf{c}^{\mathrm{II}} & \mathbf{0} & & \\ & & \ddots & & \\ & & & \mathbf{a}^{\mathrm{VI}} & -\mathbf{a}^{\mathrm{VII}} \\ & & & \mathbf{c}^{\mathrm{VI}} & -\mathbf{c}^{\mathrm{VII}} \end{bmatrix} \cdot \begin{bmatrix} \mathbf{X}^{\mathrm{I}} \\ \vdots \\ \mathbf{X}^{\mathrm{VII}} \end{bmatrix} = \begin{bmatrix} \mathbf{0} \\ \vdots \\ \mathbf{0} \end{bmatrix} \tag{31}$$

The matrix equation above only shows the coefficient matrices of the innermost and outermost regions. Since there is no current source in CMG, the right-hand side of the equation are zero matrices.

2.7 Nonlinear permeability

By utilizing the methods above, the magnetic field distribution for each region can be determined based on the initial permeability. However, if the magnetic permeability of a region significantly differs from the initial value, the magnetic induction intensity obtained may deviate substantially from the actual value. In such cases, it is important to adjust the magnetic permeability to ensure the accuracy of the results.

In this paper, Silicon steel 35WW300 is used as the material of modulator. Based on our experience, the magnetic saturation primarily occurs in the region of the modulating piece and the bridge connection. To simplify the iterative calculations, only the unit permeability in the region of the modulator ,including the modulating pieces and the bridge connection, will be iterated, while keeping the permeability in the other region constant. The iterative process is shown in the Fig.5. Initially, a magnetic field distribution is hypothesized, and the initial permeability is obtained from the *B-H* curve as shown in Fig.6. Based on this, the magnetic field distribution is determined. Then, a new permeability matrix is obtained based on the magnetic intensity *H*. If the error between the new and original permeability values is not within an acceptable range, the process is iterated until the error in magnetic permeability converges to the set acceptable range. If it exceeds the maximum number of iterations, the calculation is stopped and the results are outputted.

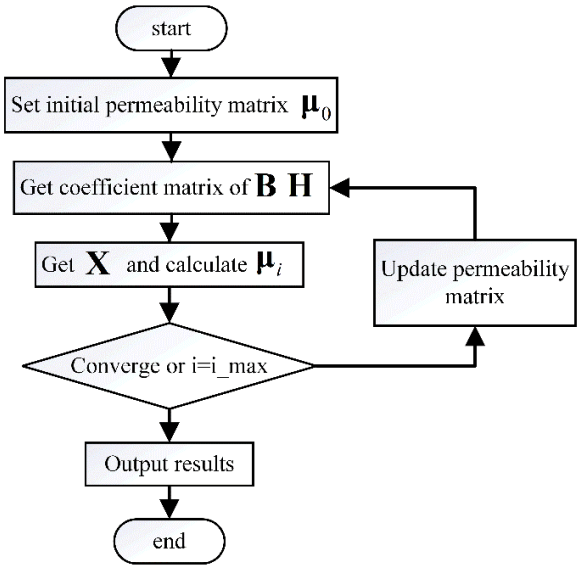

Fig.5 Flow chart of nonlinear analysis

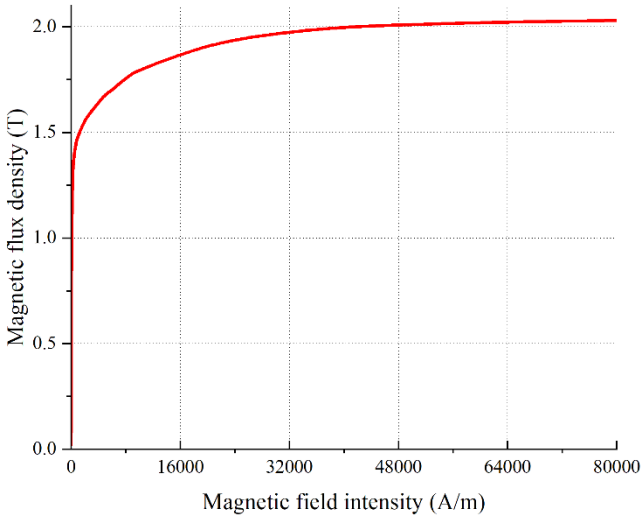

Fig.6 B-H curve of 35WW300

3. Result validation

To verify the accuracy of the calculation method, two different CMG topologies were designed, and cases with two different bridge thicknesses were calculated for each topology. In the first topology(T1), the bridge connection was located at the inner radius of the modulator (R_{b_i}=R_3). Two cases with different bridge thicknesses were set for this topology: Case 1 (T1C1) with a 2mm thickness and Case 2 (T1C2) with a 3mm thickness. The magnetic field distribution was calculated for two different thicknesses of the bridge connection (R_{b_o}-R_{b_i}), namely 2mm and 3mm. In the second topology(T2), the bridge was located at the middle radius of the modulator (R_3+R_4=R_{b_o}+R_{b_i}), and the magnetic field distribution was also calculated for two different thicknesses of the connection, 2mm and 3mm. The initial magnetic permeability of the cell division of modulator was set to 10000μ_0, and the other parameters were listed in table.1. Finite element simulation was performed on the model to obtain the distribution of the internal and external magnetic fields.

TABLE I

PARAMETERS OF THE CMG

Symbol	Value	Description
R_1	30 mm	
R_2-R_1	10 mm	thickness of PMs
R_3-R_2	1 mm	internal air gap
R_4-R_3	20 mm	thickness of modulator
R_5-R_4	1 mm	external air gap
R_6-R_5	10 mm	thickness of PMs
P_i	2	pole pairs of inner rotor
P_o	5	pole pairs of outer rotor
N_m	7	Number of modultor pieces
α, β	0.95	pole arc coefficient of PMs
θ_m, θ_b	π/14 rad	modulator angles
R_{b_i}	31 mm	topology 1
	41 mm	topology 2
R_{b_o}-R_{b_i}	2 mm	thickness case 1
	3 mm	thickness case 2

The comparison of the distribution of magnetic flux densities in the inner airgap calculated by SHMM and FEA is shown in Fig.7 to Fig.10. The magnetic flux densities distribution of the inner airgap was taken at a radius of R_{gap_i}=(R_2+R_3)/2. The radial and tangential magnetic induction intensity distributions of the airgaps obtained by using different calculation methods were in good agreement. The radial and tangential magnetic induction intensity distributions of the air gaps obtained by using different calculation methods were in good agreement. As shown in TABLE II, the calculated Mean Squared Error (MSE) between the two sets of results was found to be very small, indicating that the data are closely aligned and the results are reliable. Compared with the finite element method, consideration of the mesh division is not required by SHMM. The results demonstrate the accuracy and effectiveness of SHMM.

TABLE II

Comparison of Magnetic Field Distributions:

Mean Squared Error (MSE) Analysis

	Bri	Bti
T1C1	0.020	0.010
T1C2	0.018	0.008
T2C1	0.038	0.026
T2C2	0.036	0.026

An essential advantage of the presented numerical method lies in its computational efficiency compared to traditional finite element methods. To illustrate this, the convergence characteristics and computational time were analyzed for the different topologies considered (T1C1, T1C2, T2C1and T2C2).

The iterative nonlinear permeability adjustment typically converged rapidly, with the average number of iterations ranging from 6 to 9 across all cases. Table III summarizes the convergence details and computation times for each case.

TABLE III

Iterative Convergence and Computation Time Comparison

Topology	Bridge Thickness	SHMM Computation Time	FEA Computation Time
T1C1	2mm	0.020	0.010
T1C2	3mm	0.018	0.008
T2C1	2mm	0.038	0.026
T2C2	3mm	0.036	0.026

The results in Table III clearly demonstrate that the proposed method substantially reduces computational time, achieving approximately one order of magnitude improvement compared to the FEA method. This remarkable speed advantage primarily stems from the absence of mesh generation requirements, significantly fewer iterations for convergence, and efficient use of spatial harmonic expansions. It is particularly suitable for quick parametric analysis and optimization studies at early design stages, providing a robust basis for exploring various design scenarios without excessive computational cost.

Overall, these analyses validate not only the accuracy and reliability of the proposed method but also its substantial practical advantages in terms of computational efficiency and insightful performance evaluation.

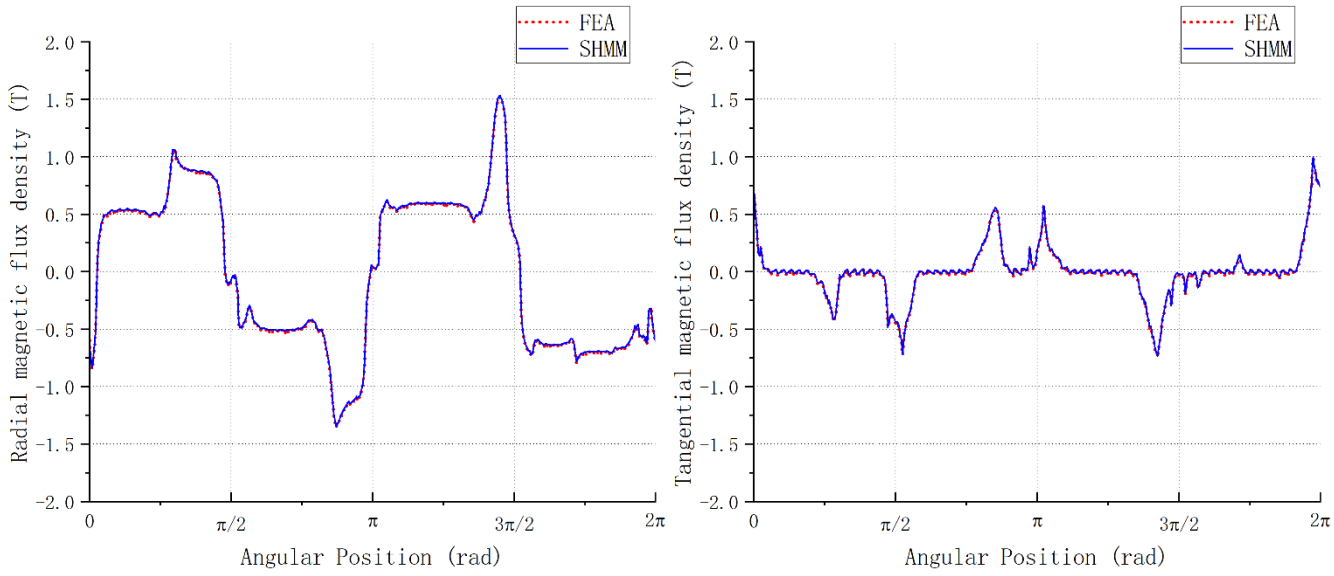

Fig.7 Comparison of the distribution of magnetic flux densities in the inner airgap calculated by SHMM and FEA in T1C1 (a) radial magnetic flux densities (b) tangential magnetic flux densities

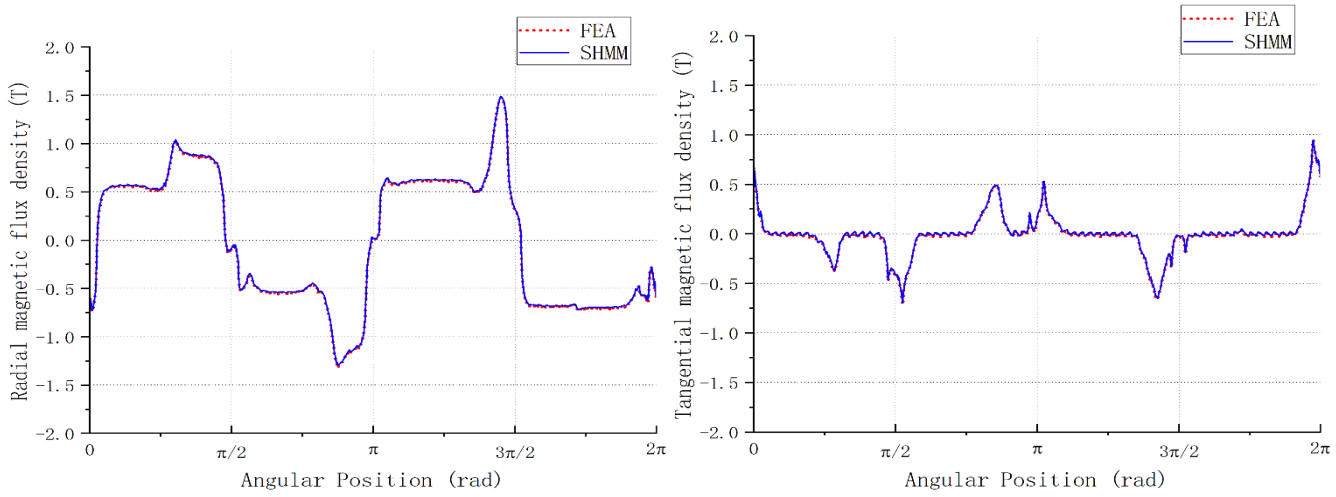

(a) radial magnetic flux densities (b) tangential magnetic flux densities

Fig.8 Comparison of the distribution of magnetic flux densities in the inner airgap calculated by SHMM and FEA in T1C2

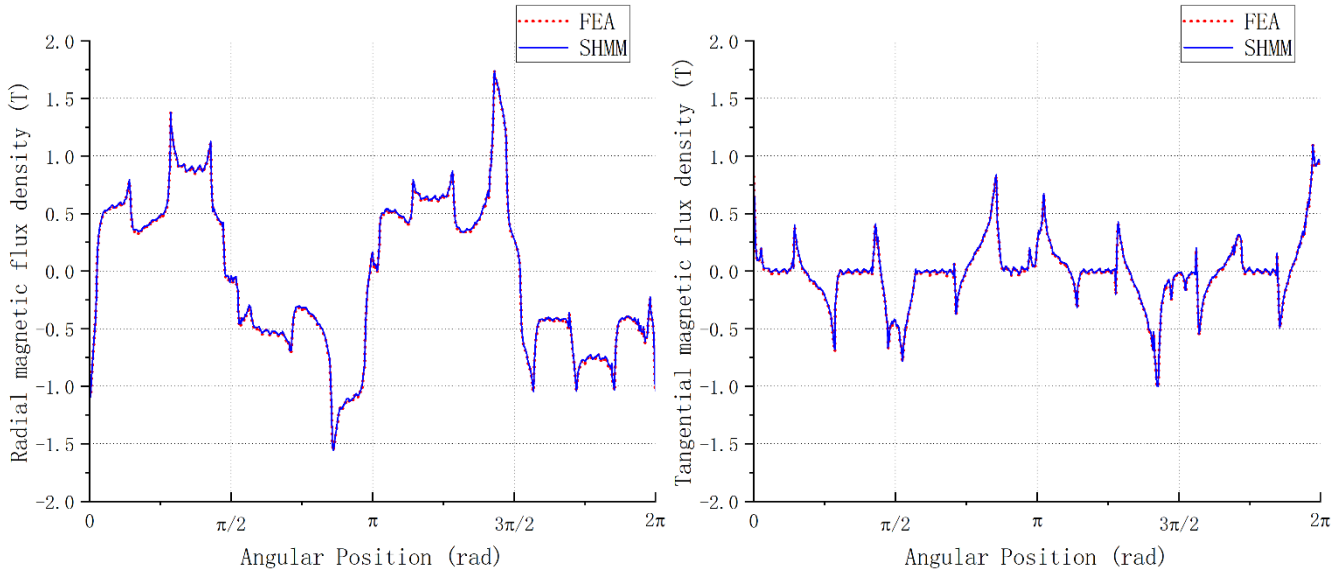

(a) radial magnetic flux densities (b) tangential magnetic flux densities

Fig.9 Comparison of the distribution of magnetic flux densities in the inner airgap calculated by SHMM and FEA in T2C1

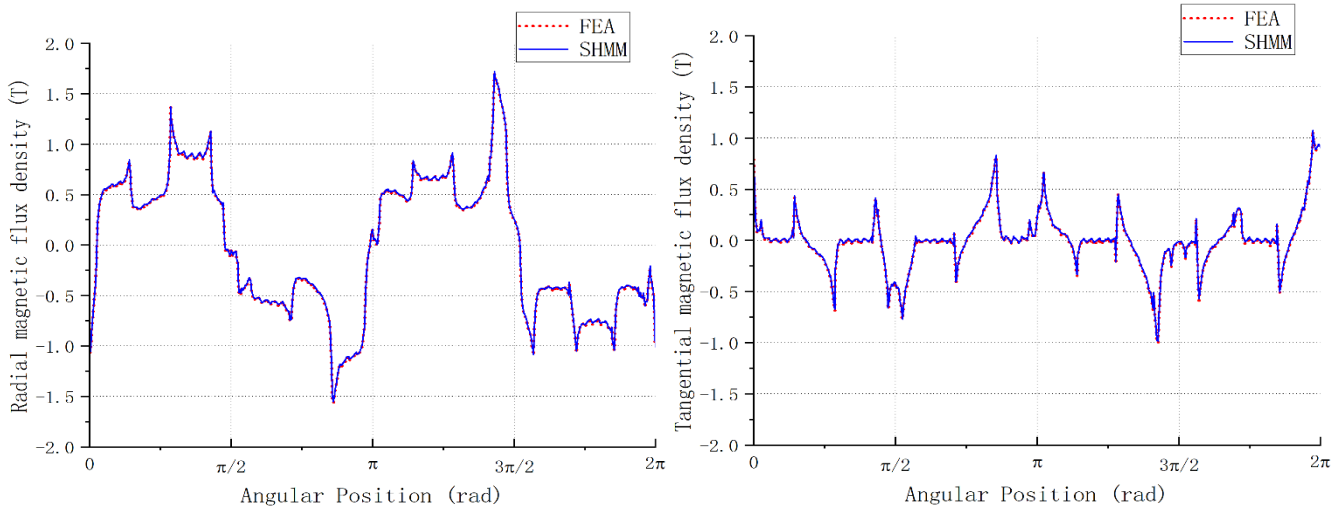

(a) radial magnetic flux densities (b) tangential magnetic flux densities

Fig.10 Comparison of the distribution of magnetic flux densities in the inner airgap calculated by SHMM and FEA in T2C1

4. Conclusion

The spatial harmonic modeling method effectively addresses the problem that the subdomain method cannot handle changes in magnetic permeability within the part area and has significant advantages for calculating cases with magnetic saturation. The proposed cell division method in this paper can be applied to modulator with different topological structures. However, as the complexity of the structure increases, cells need to be further subdivided to approximate the actual model, which increases the number of unknown parameters in the magnetic reluctance matrix and thus prolongs the calculation time. Additionally, there may be convergence issues with the calculation results, and further algorithm optimization is required for more complex cases.

Funding

This work was supported by the National Natural Science Foundation of China under Grant 52105148.

Declaration of Conflicting Interests

The author(s) declared no potential conflicts of interest with respect to the research, author-ship, and/or publication of this article.

Data Sharing Agreement

The datasets used and/or analyzed during the current study are available from the corresponding author on reasonable request.

References

[1] T. Lubin, S. Mezani, and A. Rezzoug, "Analytical Computation of the Magnetic Field Distribution in a Magnetic Gear," *IEEE Trans. Magn.*, vol. 46, no. 7, pp. 2611-2621. 2010.

[2] L. Jian and K.T.Chau. "Analytical calculation of magnetic field distribution in coaxial magnetic gears." *Progress In Electromagnetics Research* 92: 1-16. 2009.

[3] M. Lou and L. Yao, "Mathematic Modelling and Numerical Analysis for a Novel Inner-Type Nutation Magnetic Drive," *Energies*, vol. 13, no. 6, p. 1346, 2020-03-13. 2020.

[4] J. Ding, L. Yao, Z. Xie, Z. Wang, and G. Chen, "A Novel 3-D Mathematical Modeling Method on the Magnetic Field in Nutation Magnetic Gear," *IEEE Trans. Magn.*, vol. 58, no. 5, pp. 1-10. 2022.

[5] B. Dianati, H. Heydari, and S. A. Afsari, "Analytical Computation of Air-Gap Magnetic Field in a Viable Superconductive Magnetic Gear," *IEEE Trans. Appl. Supercond.*, vol. 26, no. 6, pp. 1-12. 2016.

[6] L. Jing, J. Gong, and T. Ben, "Analytical Method for Magnetic Field of Eccentric Magnetic Harmonic Gear," *IEEE Access*, vol. 8, pp. 34236-34245. 2020.

[7] R. Liu, Z. Zhao, G. Sun, Y. Mi, S. Lin, and J. Tang, "Exact magnetic field analytical model for eccentric magnetic harmonic gears using hyperbolic cotangent transformation," *IET Electr. Power Appl.*, vol. 14, no. 13, pp. 2667-2674. 2020.

[8] L. Jian, G. Xu, C. C. Mi, K. T. Chau, and C. C. Chan, "Analytical Method for Magnetic Field Calculation in a Low-Speed Permanent-Magnet Harmonic Machine," *IEEE Trans. Energy Convers.*, vol. 26, no. 3, pp. 862-870. 2011.

[9] Z. Ling, W. Zhao, J. Ji, and M. Xu, "Design and Analysis of a Magnetic Field Screw Based on 3-D Magnetic Field Modulation Theory," *IEEE Trans. Energy Convers.*, vol. 37, no. 4, pp. 2620-2628. 2022.

[10] A. Rahideh, A. A. Vahaj, M. Mardaneh, and T. Lubin, "Two-dimensional analytical investigation of the parameters and the effects of magnetisation patterns on the performance of coaxial magnetic gears," *IET Electr. Syst. Transp.*, vol. 7, no. 3, pp. 230-245. 2017.

[11] Y. Akcay, T. Cox, A. Costabeber, and G. Sala, "Analytical Model for Reluctance and Cage Rotor Bar Magnetic Gear," *IEEE Trans. Ind. Appl.*, vol. 56, no. 3, pp. 2752-2761. 2020.

[12] H. M. Shin and J. H. Chang, "Analytical Magnetic Field Calculation of Coaxial Magnetic Gear With Flux Concentrating Rotor," *IEEE Trans. Magn.*, vol. 52, no. 7, pp. 1-4. 2016.

[13] Y. Wu and B. Jian, "Magnetic field analysis of a coaxial magnetic gear mechanism by two-dimensional equivalent magnetic circuit network method and finite-element method," *Appl. Math. Model.*, vol. 39, no. 19, pp. 5746-5758. 2015.

[14] H. Lee, J. Lee, J. Woo, K. Shin, and J. Choi, "Magnetic field and torque analysis of coaxial magnetic gear using semi-analytical and superposition methods," *AIP Adv.*, vol. 13, no. 1, p. 15018, 2023-01-01. 2023.

[15] Y. Wang, M. Filippini, G. Bacco, and N. Bianchi, "Parametric Design and Optimization of Magnetic Gears With Differential Evolution Method," *IEEE Trans. Ind. Appl.*, vol. 55, no. 4, pp. 3445-3452. 2019.

[16] K. Shin, H. Park, H. Cho, and J. Choi, "Parametric analysis and optimized torque characteristics of a coaxial magnetic gear based on the subdomain analytical model," *AIP Adv.*, vol. 7, no. 5, p. 56619. 2017.

[17] L. Jing, L. Liu, M. Xiong, and D. Feng, "Parameters Analysis and Optimization Design for a Concentric Magnetic Gear Based on Sinusoidal Magnetizations," *IEEE Trans. Appl. Supercond.*, vol. 24, no. 5, pp. 1-5, 2014-01-01. 2014.

[18] D. Z. Abdelhamid and A. M. Knight, "The effect of modulating ring design on induction machine with integrated magnetic gear torque,", IEEE, 2017, pp. 1169-1174.

[19] D. Z. Abdelhamid and A. M. Knight, "The Effect of Modulating Ring Design on Magnetic Gear Torque," *IEEE Trans. Magn.*, vol. 53, no. 11, pp. 1-4. 2017.

[20] S. A. Khan, G. Duan and M. C. Gardner, "Comparison of Modulator Retention Shapes for Radial Flux Coaxial Magnetic Gears," *2022 IEEE Energy Conversion Congress and Exposition (ECCE)*, Detroit, MI, USA, , pp. 1-7. 2022.

[21] Y. Zhan, L. Ma, K. Wang, H. Zhao, G. Xu, and N. Ding, "Torque Analysis of Concentric Magnetic Gear With Interconnected Flux Modulators," *IEEE Trans. Magn.*, vol. 55, no. 6, pp. 1-4. 2019.

[22] H. Zhao, C. Liu, Z. Song, and J. Yu, "A Fast Optimization Scheme of Coaxial Magnetic Gears Based on Exact Analytical Model Considering Magnetic Saturation," *IEEE Trans. Ind. Appl.*, vol. 57, no. 1, pp. 437-447. 2021.

[23] R. L. J. Sprangers, J. J. H. Paulides, B. L. J. Gysen, and E. A. Lomonova, "Magnetic Saturation in Semi-Analytical Harmonic Modeling for Electric Machine Analysis," *IEEE Trans. Magn.*, vol. 52, no. 2, pp. 1-10. 2016.